# Device Applications of Silicon Nanocrystals and Nanostructures

Nanostructure Science and Technology

Series Editor: David J. Lockwood, FRSC
*National Research Council of Canada*
*Ottawa, Ontario, Canada*

For other titles published in this series, go to
www.springer.com/series/6331

Nobuyoshi Koshida
Editor

# Device Applications of Silicon Nanocrystals and Nanostructures

Springer

*Editor*
Nobuyoshi Koshida
Department of Electrical & Electronic Engineering
Tokyo University of Agriculture and Technology
Tokyo, Japan

ISBN: 978-0-387-78688-9 e-ISBN: 978-0-387-78689-6
DOI: 10.1007/978-0-387-78689-6

Library of Congress Control Number: 2008940837



Printed on acid-free paper

springer.com

# Foreword

Silicon: Different people associate the word with different things. The general public will often correctly link it to electronics and sometimes confuse it with the compound that seals their bath or enlarges particular body parts. As scientists or technologists, we know the elemental semiconducting version to be one of, if not, the most studied materials known. But when we sculpt solid silicon structures below 10 nm, a variety of dramatic and often astonishing effects ensue.

Indeed, this book on nanostructured silicon devices brings together two of the great endeavours of our generation. There has already been huge investment and human ingenuity in the pervasive silicon device – the integrated circuit. There is now also mounting excitement and investment in nanotechnology – our ability to design, fabricate, and use techniques and materials at the nanoscale.

The book's editor, Professor Nobuyoshi Koshida, is undoubtedly a great pioneer in this field, with more than 30 years of world-leading research on novel phenomena, characterization, and uses of nanoscale silicon. He has assembled a great team of authors, all established experts in their respective areas of specialization.

The content of this book show a bias toward electronic chip-based uses of "nano-silicon" (Chaps. 5–8), and rightly so. Indeed many would argue that we are only interested in silicon nanostructures because of what the bulk material has achieved with its integrated circuits inside everyone's PC, and what we hope MEMS technology might achieve. Nonetheless, within the book, one also will find significant progress toward using nano-silicon in scientific fields that might not be an obvious choice for this semiconductor. Examples are optics/photonics (Chaps. 1 and 3), optoelectronics and displays (Chaps. 2, 4, 9), biological diagnostics (Chap. 10), and ultrasonics (Chap. 11).

The interest in nanoscale silicon grew dramatically in the early 1990s and continues almost 20 years later, but in a diversified manner. The wonderfully dramatic effects of quantum confinement have enriched what was already a fairly versatile material – the additional effects of nanoscale porosity allowing tunability of many of its properties over ranges that were thought impossible.

In this book, you will discover how we now can manipulate current transport and charge in assemblies of nanocrystals at incredibly small dimensions, enabling various novel electronic devices to be realized. We can nanostructure pure silicon to be pink, green, red, or any color you like. It can be used to detect and distinguish biomolecules at very low concentrations. It can emit visible light at high efficiency. It can generate music from electrical signals. From my own studies, it can be biodegradable in the human body and thus used medically. It may even have nutritional uses in food. It is a material that continues to surprise us with its expanding potential.

Malvern, UK Leigh Canham

# Preface

Semiconductors exhibit a critical size at which quantum confinement effects become apparent. A measure of this condition is the exciton Bohr radius. This value in single-crystalline silicon is below 5 nm, which is exceptionally small in comparison to most conventional semiconductors, and is one reason why the development of silicon-based logic and memory devices has followed an anticipated road map. In fact, however, silicon devices have evolved in all stages of the design, processing, and fabrication technologies. The scaling principle is the engine driving these advances in integrated circuitry.

The scaling of advanced MOS technology is now entering the region of 10 nm. As the scaling extends to the region below the quantum-size criterion, it should be noted that the original optical, electrical, thermal, and chemical properties of bulk silicon are substantially modified. As a consequence, various useful functions are induced in quantum-sized nanocrystalline or nanostructured silicon materials. For instance, a significant band gap widening and delocalization of carriers in momentum space make the optical property free from the traditional direct or indirect-transition regime. Efficient visible luminescence is created and opens the door toward integrated silicon photonics. In addition, the range of possible applications in quantum-sized silicon is extending to the field of electronics, acoustics, and biology.

The main theme of this book is how widely the potential functions of silicon have been implemented as devices in the nanometer region, and that silicon devices in the quantum zone produce various technological values different from the scaling merits. The volume is composed of three main subjects: photonic devices (four chapters), electronic devices (five chapters), and functional devices (two chapters).

In the first four chapters, basic characterization of silicon-rich dielectrics for photonic uses are addressed followed by the development of silicon electroluminescence devices as a key issue for monolithic integration. The succeeding two chapters describe fabrication and properties of periodic silicon nanostructures as an important photonic component as well as analyses of possible optical gain in silicon system leading to a breakthrough in this field.

The next five chapters are devoted to state-of-the-art work on electronic devices based on nanostructures: single-electron device, spin transistor, specified electron transport in nanosilicon dot chains, nonvolatile information storage, and surface-emitting ballistic cold cathode. These topics suggest the range of forthcoming electronic device applications. The last two chapters concern the applicability of nanostructured silicon layers to functional biosensing scaffold and to thermally induced ultrasound emission. The former and the latter come from the biocompatible nontoxic features and complete thermal insulating properties of nanoscale silicon, respectively.

As demonstrated in all chapters, the key word common to nanocrystalline or nanostructured silicon is functionality as a technology platform for next-generation devices. Hopefully, this book gives a perspective on the device image in the posts-caling era, since silicon technology should be further amplified by functional integration in which photonic, electronic, acoustic, and biological functions are involved in conjunction with advanced ULSI devices.

Tokyo, June 2008 Nobuyoshi Koshida

# Acknowledgments

The editor thanks all coauthors of this book for the stimulated and careful preparation of their manuscript and artwork. It was great to have an opportunity of fruitful cooperation with many colleagues during this project. Thanks are due to Dr. D.J. Lockwood, the series editor of Nanostructure Science and Technology, for his encouraging suggestions in the progress of this work and to Prof. L.T. Canham for his continuing and invaluable communications. The production of this book is totally owing to patient, competent, and helpful support of Anushka Hosain, Lee Lubarsky, and Dr. David Packer at Springer.

# Contents

# 1

# Si-Rich Dielectrics for Active Photonic Devices

L. C. Kimerling*, L. Dal Negro†, M. Stolfi, J. H. Yi, J. Michel, X. Duan, E. H. Sargent, T.-W. F. Chang, V. Sukhovatkin, J. Haavisto, and J. LeBlanc

**Abstract** The quest to develop an efficient Si-based light emitter has stimulated research worldwide. Among the several approaches being considered, enhancing the probability of light emission through the use of Si nanocrystals embedded in $SiO_2$ shows considerable promise due to the demonstration of efficient room temperature light emission and optical gain. In this chapter, we compare the nucleation, light emission, and emission sensitization of Si nanocrystals embedded in Si-rich oxide and Si-rich nitride. Based on the results of our study, we identify Si nanocrystal emission from Si-rich nitride and Er doping of Si-rich oxide as materials systems that satisfy the requirements of CMOS compatible processing and high emission efficiency for integration with Si-based electronics. We also present PbS quantum dot emission sensitization through Si nanocrystals in Si-rich nitride, an alternative approach to achieving efficient infrared emission on a Si platform. The improved electrical properties and high refractive index of Si-rich nitride also allows for the fabrication of electroluminescent devices with small footprints and active, complex photonic crystal devices for multiwavelength applications.

## 1. INTRODUCTION

The trend of improving microprocessor performance through size scaling has revealed several challenges that threaten the microelectronics industry's ability to follow Moore's law. Large RC delays and heat dissipation produced by closely

* Massachusetts Institute of Technology, 77 Massachusetts Avenue, Cambridge, MA 02139-4307, USA, lckim@mit.edu

† Department of Electrical and Computer Engineering, Boston University, Boston, Massachusetts 02215 and Materials Science Division, Boston University, Boston, Massachusetts 02215

N. Koshida (ed.), *Device Applications of Silicon Nanocrystals and Nanostructures*,
DOI: 10.1007/978-0-387-78689-6_1, 

spaced, small cross-sectional metal interconnects have replaced transistor gate delays as the primary limiting factor in improving performance and in stimulating the development of novel approaches for device interconnection. Si microphotonics, the monolithic integration of Si-based optics and electronics, is one approach to device interconnection that offers significantly improved bandwidth with negligible heat dissipation and cross-talk to achieve high clock speeds and low latency interconnection between microprocessors operating in parallel. Optical interconnection, when applied to the telecommunications industry, led to improvements of several orders of magnitude in information capacity. Several of the building blocks required to apply this technology to electrical integrated circuits have recently been demonstrated in Si including low loss optical waveguides for interconnection [1], optical modulation [2], and switching [3].

Missing is an efficient Si-based light emitter. It is well known that Si is an indirect bandgap material where photon emission originates from low-probability, phonon-mediated transitions that compete unfavorably with fast, nonradiative de-excitation paths, such as Auger recombination and free carrier absorption. As a result, the only reports of lasing in Si are based on stimulated Raman scattering, which suffers from a high threshold and low wall-plug efficiency [4, 5]. To overcome the limitations for light emission in Si several strategies have been recently developed to engineer Si into a more efficient light emitting material [6–10]. The approach of quantum confinement has led to a dramatic improvement of the light generation efficiency in Si nanostructures [9–12]. The high emission efficiencies of up to 23% under optical excitation reported in porous Si after high pressure water vapor annealing [12], integration of a porous Si light emitting diode and bipolar transistor [13], and sizeable optical gain recently demonstrated in Si nanocrystals embedded in $SiO_2$ matrices [14–19] have opened the race toward the fabrication of an integrated, fully Si-based laser [9]. Moreover, it has been recently discovered that Si nanocrystals act as efficient emission sensitizers for rare-earth ions, particularly Er ions, allowing broad band pumping of 1.54 μm light emission with almost three orders of magnitude-enhanced pumping efficiency [20–25].

With sizes ranging from 1 to 10 nm Si nanocrystal systems possess high surface to volume ratios. Therefore, it is no surprise that the interface between the Si nanocrystal and the surrounding matrix plays a crucial role in determining the optical properties of Si nanocrystals. In particular, the presence of Si&dbond;O bonds [26–29] at the surface of small Si nanocrystals embedded in Si-rich oxide is believed to have a dramatic impact on the light emission properties of these systems. This opens the possibility of engineering the interface properties through the controlled addition of dopants or changing the surrounding dielectric matrix entirely. An intriguing possibility would be the nucleation of Si nanocrystals in dielectric matrices with smaller bandgaps than $SiO_2$, and more favorable electrical properties compared to traditional devices based on porous Si and Si nanocrystals embedded in $SiO_2$ matrices. Following this approach, visible and near-infrared light emitting Si nanocrystals embedded in $Si_3N_4$ matrices have been recently demonstrated [30, 31] and efficient visible electroluminescence has been reported [32, 33].

In this chapter, we report on a comparison between the formation and properties of Si nanocrystals fabricated in Si-rich oxide and Si-rich nitride. There are three

objectives to our study (1) obtaining a deeper understanding of the processes leading to efficient light emission and emission sensitization, (2) optimizing the fabrication conditions with respect to performance, and (3) investigating novel applications and devices based on Si nanocrystals including energy transfer to PbS quantum dots and active photonic crystals. The standards we use to determine optimum performance are (1) CMOS compatibility, using standard CMOS processing techniques with a low thermal budget; (2) high emission efficiency; and (3) in the case of electrically driven devices, stable operation and high injection efficiency at low voltages.

## 2. NUCLEATION AND STRUCTURAL PROPERTIES OF SI NANOCRYSTALS

Si nanocrystals have been produced through several techniques including annealing of Si-rich oxide [34–39], electrochemical etching [6, 40], laser-assisted processing [41, 42], solution synthesis [43], and annealing of $Si/SiO_2$ [44] or $SiO/SiO_2$ superlattices [45]. In this chapter, we will focus on the fabrication of Si nanocrystal devices through annealing of Si-rich oxides and nitrides. Si-rich oxide can be fabricated through a variety of techniques such as ion implantation into stoichiometric $SiO_2$ [35, 36], chemical vapor deposition [34, 37], sputtering [38], and thermal evaporation of SiO [39]. After deposition, the films are annealed to induce a precipitation transformation where the metastable Si-rich dielectric film decomposes into two stable phases: Si clusters and a matrix, which is closer in composition to the equilibrium (stoichiometric) composition. According to classical nucleation theory [46, 47] the driving force for the precipitation transformation is a volume free energy reduction, $\Delta G_v(X_{Si},T_A)$, which increases as the Si content is increased above the stoichiometric level (given by the mole fraction of Si, $X_{Si}$) and the annealing temperature, $T_A$, is increased. Opposing the volume free energy reduction is the energy required to create the interface between the Si cluster and the matrix, $A\gamma_{CM}$, where $A$ is the surface area and $\gamma_{CM}$ is the cluster–matrix interfacial energy. The total free energy passes through a maximum as a function of cluster radius where the maximum is associated with the free energy to form a critical nucleus, which is given by the expression $\Delta G^* = \left(16\pi\gamma_{CM}^3\right)\!\!\Big/ 3\Delta G_v^2$ for spherical clusters with a critical cluster radius of $r^* = 2\gamma_{CM} / \Delta G_v$. In homogeneous nucleation, all of the energy required to form the cluster–matrix interface must be supplied by the chemical driving force, as described above. However, in most real systems the nucleation occurs through heterogeneous nucleation at pre-existing defect sites where the threshold for nucleation is reduced by the energy released through the annihilation of the defect. In either case, once nucleation occurs with the formation of critically sized nuclei, cluster growth is governed by the process of coarsening, which minimizes the overall surface energy of the system by promoting the growth of large clusters at the expense of smaller clusters. By considering these principles of nucleation and growth, the parameters of Si content, annealing temperature, and annealing time can be used to fabricate nanocrystal ensembles with the desired size and density. For example, the theory predicts the highest density of small Si nanocrystals for low annealing temperatures. We will describe in the following sections how the fabrication conditions of Si content, annealing temperature, and annealing time are

important for the fabrication of nanocrystal ensembles with high quantum efficiency, strong emission sensitization, and high electrical injection efficiency.

To investigate the formation of Si nanocrystals we have prepared Si-rich nitride thin films through plasma-enhanced chemical vapor deposition (PECVD) and magnetron co-sputtering and Si-rich oxide thin films through reactive magnetron sputtering. The PECVD nitride films were fabricated using an Applied Materials Centura DxZ chamber with $SiH_4$ and $N_2$ as precursors and a substrate temperature of 400°C. The sputtering was performed, without substrate heating, in a Kurt J. Lesker Co. CMS-18 system. For the Si-rich nitride films, the sputter deposition was performed using Si and $Si_3N_4$ targets in an Ar atmosphere. For the Si-rich oxide films, the sputter deposition was performed reactively using a Si target in an $O_2$/Ar atmosphere. We used Raman spectroscopy to examine the evolution of the Si-rich dielectric matrix with annealing conditions since amorphous and crystalline Si structures have unique Raman signatures [48].

Both unannealed Si-rich nitride and unannealed Si-rich oxide (Fig. 1a, b; dotted line) show a broad Raman band due to an amorphous Si network while an additional broadened, asymmetric, and shifted Raman peak (with respect to bulk Si) can be clearly observed for annealed samples (Fig. 2a, b; dashed line). For the annealed, PECVD-deposited Si-rich nitride sample, three peaks can be distinguished in Fig. 1a corresponding to the two-phonon acoustical (~300 $cm^{-1}$) and optical (~900 $cm^{-1}$) scattering bands as well as the one phonon band at 512 $cm^{-1}$. We also note that for the PECVD Si-rich nitride sample after annealing, the two-phonon optical (~900 $cm^{-1}$) and acoustical (~300 $cm^{-1}$) scattering bands are strongly enhanced with respect to both the bulk Si and the unannealed sputtered Si-rich nitride sample. The presence of a significantly shifted ($\Delta\nu$ ~ 15 $cm^{-1}$) and asymmetrized one-phonon Raman peak for annealed, PECVD-deposited Si-rich nitride and annealed, sputtered

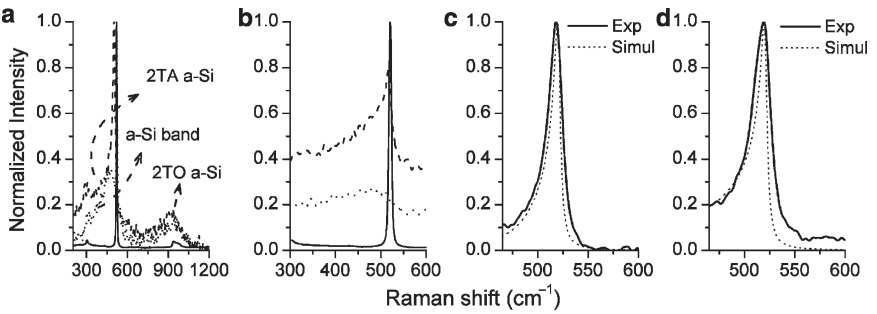


FIG. 1. (**a**) Micro-Raman spectra of crystalline Si (*solid line*), unannealed Si-rich nitride deposited by sputtering (*dotted line*), and PECVD deposited Si-rich nitride annealed at 700°C for 10 min (*dashed line*). (**b**) Micro-Raman spectra of crystalline silicon (*solid line*), unannealed Si-rich oxide deposited by sputtering (*dotted line*), and Si-rich oxide deposited by sputtering annealed at 1,100°C for 1 h (*dashed line*). (**c**) Micro-Raman spectrum of Si nanocrystals embedded in $SiO_2$ annealed at 1,100°C for 1 h (*solid line*). Theoretical simulation assuming ~6 nm average crystal diameter (*dotted line*). (**d**) Micro-Raman spectrum of Si nanocrystals embedded in amorphous $Si_3N_4$ annealed at 700°C for 10 min (*solid line*). Theoretical simulation assuming 2-nm average crystal diameter (*dotted line*).

Si-rich oxide is the direct evidence of the formation of small Si clusters embedded in the amorphous dielectric matrix. The physical origin of the broadened Si peak is related to the uncertainty in the Si-cluster phonon momentum, $q$, that allows modes with $q \neq 0$ to contribute in the Raman spectrum. This general physical picture, referred to as phonon bottleneck, can be quantitatively described within a phenomenological model that accounts for the line shape of the TO one-phonon modes of quantum-confined Si clusters [49]. The one-phonon Raman line shapes can be easily obtained by calculating the integral transform [50]

$$I(\omega) = \int_0^1 \frac{e^{-qL^2/4a^2}}{[\omega - \omega(q)]^2 + (\Gamma_0/2)^2} d^3q, \quad (1)$$

where $L$ is the average Si nanocrystal radius, $\Gamma_0$ is the linewidth of the LO bulk Si phonon, and $a$ is the Si lattice constant. The phonon dispersion of the bulk material is given by the relation $\omega^2(q) = A + B\cos(\Pi q / 2)$ with $A = 1.714 \times 10^5$ cm$^{-2}$ and $B = 1.000 \times 10^5$ cm$^{-2}$ [50, 51]. This phenomenological approach allows us to simulate the experimental Raman data and to estimate an average size for the quantum confined scattering particles.

We have applied this procedure to the Si-rich oxide sample annealed at 1,100°C for 1 h and the Si-rich nitride sample annealed at 700°C for 10 min. In the case of annealed Si-rich oxide (Fig. 1c), we estimate an average diameter of ~6 nm, while in the case of annealed Si-rich nitride (Fig. 1d), the micro-Raman data are compatible with the presence of smaller Si clusters with an estimated diameter less than 2 nm, as fitted within the phonon confinement Raman model. To check the consistency of this analysis, the nanocrystal sizes were observed through transmission electron microscopy (Fig. 2). The average diameters determined from the

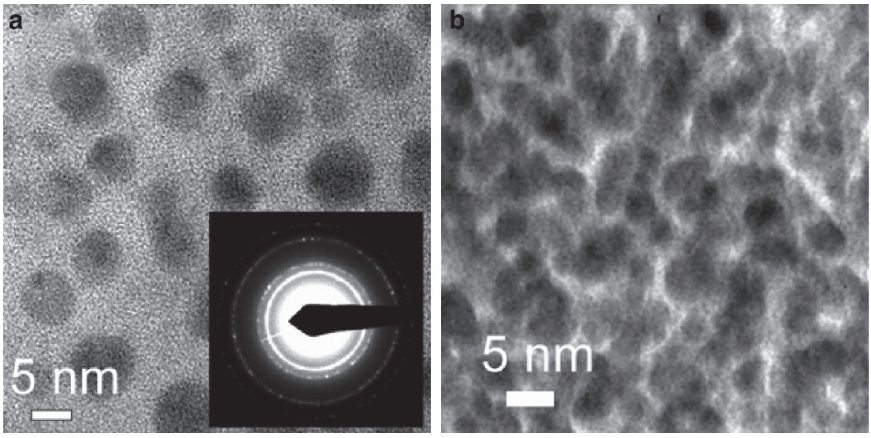


FIG. 2. (**a**) Plan view transmission electron microscope image of Si nanocrystals (*dark spots*) with an average diameter of 6 nm embedded in Si-rich oxide annealed at 1,100°C for 1 h. (**b**) Cross-section transmission electron microscope image of Si nanocrystals (*dark spots*) with an average diameter of ~1–2 nm embedded in Si-rich nitride annealed at 700°C for 10 min.

electron micrographs were 6 nm for Si-rich oxide and ~1–2 nm for Si-rich nitride in perfect agreement with the analysis of the Raman spectra.

## 3. OPTICAL PROPERTIES OF SI NANOCRYSTALS

Based on the different sizes, densities, and formation conditions for our Si nanocrystals in oxides and nitrides, we can expect that their optical properties and the optimization of those properties may also be different. This is generally true for Si nanocrystals that have been produced through a variety of techniques due to the sensitivity of the nanocrystal performance on the details of the sample preparation [52]. Before discussing the comparison of the optical properties of our nanocrystals, we will review the optical properties of Si nanocrystals in oxide systems which have been investigated extensively. Si nanocrystals possess several intriguing optical properties with application toward the fabrication of optoelectronic devices. Among these is a broad, near infrared emission spectrum, located above the band edge of bulk Si, with a peak emission wavelength that can be tuned over a few hundred nanometers by varying processing parameters [41, 53, 54]. Several studies have been conducted to understand the origin of this strong emission. Time-resolved photoluminescence experiments have revealed a stretched exponential decay of the nanocrystal emission with a decay time in the range of 10–100 μs [55]. The stretched exponential decay is caused by energy migration from small Si nanocrystals to large Si nanocrystals with the degree to which the exponential is stretched decreasing with increasing excitation wavelength (selectively exciting progressively larger nanocrystals) [56]. Emission experiments performed on single Si nanocrystals have revealed a homogeneous linewidth of 100–150 meV at room temperature; the typical spectral width, which can be as large as 500 meV, is therefore dominated by inhomogeneous broadening due to the broad size and shape distributions that exist in typical Si nanocrystal ensembles [57]. Despite the strong luminescence from Si nanocrystals, it has been shown through spectral hole burning experiments that the indirect bandgap properties of bulk Si are still retained in Si nanocrystals [58]. The effect of quantum confinement of excitons within the Si nanocrystal is to increase the energy gap leading to a decrease in the emission wavelength and enhance the probability of no-phonon radiative recombination. In general, the trend of emission energy vs. nanocrystal size follows a model consistent with quantum confinement for large nanocrystals. For small nanocrystals, it has been observed that the emission energy does not increase beyond 2 eV although the nanocrystal size is decreased. Wolkin et al. [26] attributed this pinning of the bandgap to exciton recombination via Si=O bonds located at the nanocrystal/oxide interface. The sensitivity of the optical properties to the nanocrystal surface chemistry was further examined by Pudzer et al. [28] revealing the complex interplay between size and surface effects.

Co-doping of Er with Si nanocrystals can also have several positive consequences for the fabrication of Er light emitting devices. Conventional Er-doped waveguide amplifiers require intense optical pumping at discrete wavelengths due

to the small absorption cross sections corresponding to the atomic energy levels of Er. When co-doped with Si nanocrystals, Er excitation occurs via the nanocrystals with the nanocrystals absorbing the pump light and transferring the excitation to the Er with dramatic results [20–25]. The excitation cross section of Er is enhanced by as much as 1,000× with respect to Er in stoichiometric $SiO_2$ (Er:$SiO_2$) [24]. Additionally, since the excitation is occurring through the nanocrystals, any pump wavelength within the nanocrystal absorption band can be used to efficiently excite the Er ions allowing for optical pumping via white light or LED sources [59, 60]. Electroluminescent devices have also been demonstrated [61, 62]. In addition to investigating the sensitization properties of Si nanocrystals, several recent studies have been devoted to understanding the origin of enhanced emission sensitization from Si-rich oxide samples annealed at low temperatures (<800°C) [63–65]. These experimental observations open the possibility of achieving efficient Er light emitting devices with improved CMOS compatibility.

### *3.1. Si Nanocrystal Emission*

In the following sections, we will review our principal results concerning the optical emission properties of thermally annealed Si-rich nitride films deposited by PECVD and Si-rich oxide films deposited by reactive sputtering. Figure 3 summarizes the effect of film composition and postdeposition annealing temperature on the emission intensity of Si-rich nitride and Si-rich oxide samples [64, 66]. The film composition was measured through the sample refractive index using a Metricon 2010 Prism Coupler since the index of refraction increases as the excess Si content of the film increases.

In Fig. 3a, we show the photoluminescence spectra for annealed Si-rich oxide which are characterized by a broad, featureless band with tunability of the peak emission wavelength of 50 nm around the emission wavelength of 800 nm for varying film composition. The trends of the integrated photoluminescence intensity vs. the Si-rich oxide film refractive indices (Fig. 3b) and the integrated photoluminescence intensity vs. the postdeposition annealing temperature (Fig. 3c) show that the maximum is for films with refractive index = 1.7 annealed at 1,150°C for 1 h. Figure 3d shows a representative spectrum for an annealed Si-rich nitride sample. In comparison with the results obtained for Si-rich oxide, a similar study for Si-rich nitride (Fig. 3e, f) shows that the maximum light emission is obtained for samples with the highest Si content (refractive index $n = 2.2$), after thermal annealing at 700°C for 10 min. Another important feature of light emitting Si-rich nitride films, not shown here, is that both the emission wavelength and emission line shape are almost independent of the annealing temperature and the annealing time. A very weak peak shift was observed by changing the Si-rich nitride index of refraction (Si content) in the range from 2.01 to 2.24, while the emission of the stoichiometric silicon nitride ($n = 2.01$) was too weak to be detected. The lack of emission tunability observed in our Si-rich nitride systems strongly indicates that the origin of light emission is not determined by size-dependent quantum confinement effects [67].

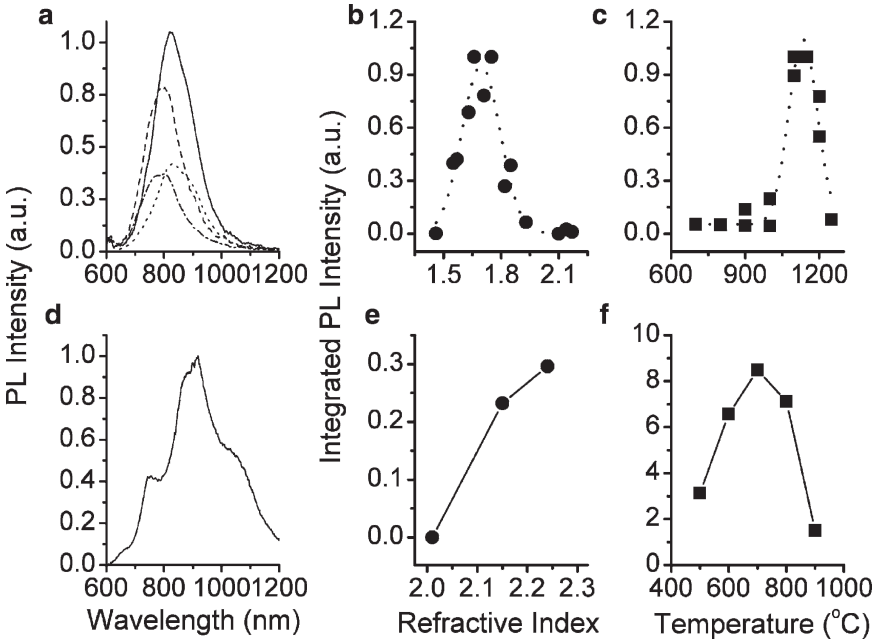


FIG. 3. (**a**) Photoluminescence spectra for Si-rich oxide annealed at 1,100°C for 1 h with the following indices of refraction: 1.62 (*dashed-dotted line*), 1.68 (*dashed line*), 1.72 (*solid line*), and 1.85 (*dotted line*). (**b**) Integrated photoluminescence intensity vs. refractive index for Si-rich oxide films annealed at 1,100°C for 1 h. (**c**) Integrated photoluminescence intensity vs. annealing temperature for Si-rich oxide films with $n = 1.7$ refractive index annealed for 1 h. (**d**) Photoluminescence spectrum for Si-rich nitride with an index of refraction of 2.2 annealed at 700°C for 10 min. (**e**) Integrated photoluminescence intensity vs. refractive index for Si-rich nitride films annealed at 700°C for 10 min. (**f**) Integrated photoluminescence intensity vs. annealing temperature for Si-rich nitride films with $n = 2.2$ refractive index annealed for 10 min.

In order to quantitatively compare the emission efficiency of Si-rich oxide vs. Si-rich nitride light emitting systems, we have measured the external photoluminescence quantum efficiency of the best emitting Si-rich nitride sample ($n = 2.2$, 700°C, 10 min) and Si-rich oxide sample ($n = 1.7$, 1,150°C, 1 h). A photoluminescence quantum efficiency of 7% was measured for the Si-rich nitride sample, following the procedure described in [68, 69]. In the case of the optimized Si-rich oxide sample, a photoluminescence quantum efficiency of 4.5% was obtained. Time-dependent photoluminescence experiments have also revealed that the Si-rich nitride lifetime (Fig. 4c) is described by a double exponential function with a resolution-limited, subnanosecond fast decay component and a longer decay component that ranges between 1 and 5 ns, depending on the observation wavelength [67]. This decay time is significantly faster than the decay time for a Si-rich oxide sample (Fig. 4d) which is 180 µs.

In Fig. 4a, b we show a direct comparison of the 7% efficient, near-infrared Si-rich nitride emission spectrum and the optical transmission spectrum. It is clear

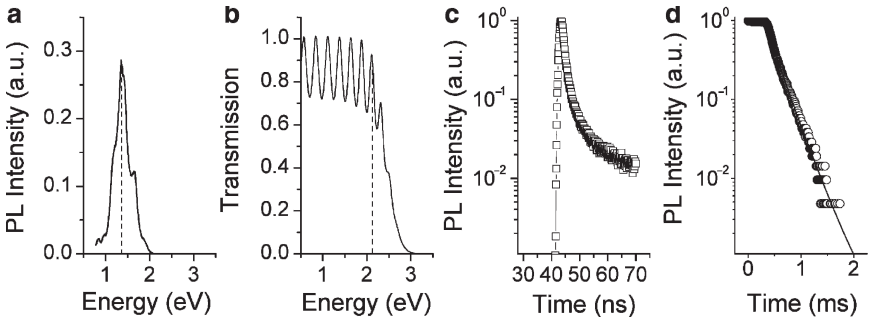


FIG. 4. (**a**) Room temperature photoluminescence spectrum of a Si-rich nitride sample annealed for 10 min at 700°C. The pump power was 5 mW at 488 nm. The *dashed line* corresponds to the peak emission energy of 1.35 eV. (**b**) Typical transmission spectrum of a Si-rich nitride sample annealed at 700°C for 10 min. The oscillations in the spectrum are due to Fabry-Perot wave interference related to the finite sample thickness (700 nm). The *dashed line* corresponds to the absorption edge of ~2 eV (**c**) Typical photoluminescence decay curve observed at 710 nm (*open squares*) fitted using a double exponential decay curve with a fast component of ~0.5 ns and a slow component of ~3 ns (*solid line*). (**d**) Typical photoluminescence decay curve observed at 900 nm (*open circles*) for Si nanocrystals in Si-rich oxide fitted using a stretched exponential decay curve with a lifetime $\tau = 180\,\mu s$ and a stretching parameter $\beta = 0.88$ (*solid line*).

that the emission band (Fig. 4a) is strongly Stokes-shifted with respect to the onset of the measured absorption edge (Fig. 4b) suggesting the strongly localized nature of the emitting centers. To investigate how the structure of the cluster and the bonds at the interface can influence the optical properties of Si-rich nitride materials, a series of density functional theory (DFT) calculations [70–72] were performed, within the local density approximation [73] (LDA) of the structural, electronic, and optical properties of Si nanoclusters with single nitrogen atoms bonded to their surface and in their core in different configurations [74]. To determine which structure(s) are most likely to be responsible for the luminescence observed in Si-rich nitride, the energy gap between the Highest Occupied Molecular Orbital (HOMO) and Lowest Unoccupied Molecular Orbital (LUMO) and the radiative lifetime for the HOMO-LUMO transition were calculated and compared with the values determined experimentally. Seven structures with a diamond crystalline core and three structures with an amorphous core, generated using ab initio molecular dynamics simulations [52], were considered with their properties calculated for different surface terminations. The structure, which most closely matched the optical properties of the Si-rich nitride material, is a diamond crystal core with a surface NH group bonded to two neighboring Si atoms, forming in both clusters a bridged Si–NH–Si structure reminiscent of disilazane. Therefore, light emission in Si-rich nitride originates from strongly localized, nitrogen-related exciton states at the surface of small (~1–2 nm) Si clusters embedded in an amorphous $Si_3N_4$ network [74].

The temperature behavior of the Si-rich nitride and Si-rich oxide light emission is shown in Fig. 5. The temperature dependence of Si-rich oxide light emission (Fig. 5b) [64] is consistent with the relative population of singlet and triplet states in agreement with the results of Brongersma et al. [75]. On the other hand, we found that the Si-rich nitride emission shows small temperature quenching (approximately a factor of 4) over a wide temperature range from 4 K up to 330 K [67]. In addition, no appreciable emission lineshape modifications have been observed (Fig. 5a; inset).

The temperature-dependent photoluminescence data for Si-rich nitride can be described by using a simple phenomenological model based on the thermal ionization of localized carriers from a radiative nitrogen defect state, as in [76]. We associate the microscopic nature of the radiative nitrogen defects suggested in [76] to the strongly localized energy state introduced by surface nitrogen bridging configurations within the molecular bandgap of small Si clusters embedded in the nitride matrix [74]. According to this interpretation, the fast, subnanosecond photoluminescence decay component is associated with a nonradiative exciton trapping time on the nitrogen sites while the longer (ns) decay results from the localized exciton recombination time.

Since the photoluminescence intensity is controlled by a competitive interplay between the nucleation of luminescent Si clusters with different sizes, emission efficiencies, and cluster densities our data indicate that a major difference exists between Si-rich nitride and Si-rich oxide light emitting systems. The fact that the optimum annealing temperature is higher and the annealing time is longer to maximize the Si nanocrystal light emission in Si-rich oxide systems compared to what is required to activate efficient light emission in Si-rich nitride systems suggests that the growth kinetics in Si-rich nitride films favors the formation of smaller Si clusters at a faster rate and for lower supersaturation than for the Si-rich oxide case.

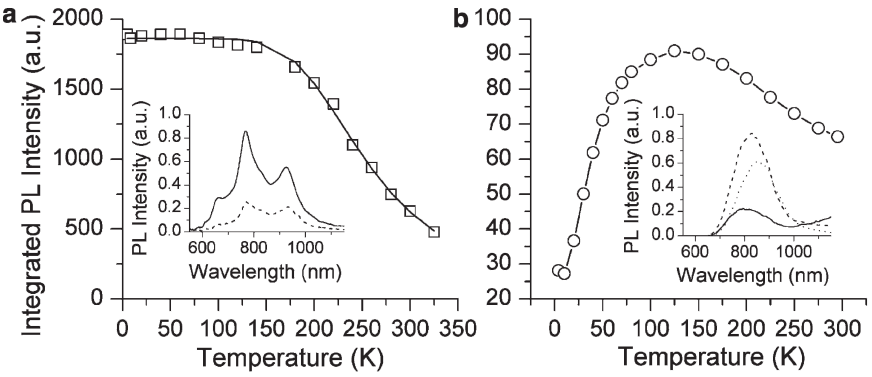


FIG. 5. (**a**) Integrated photoluminescence intensity vs. temperature for the best emitting Si-rich nitride sample ($n = 2.2$, annealed for 10 min at 700°C) (*inset*). Si-rich nitride emission spectra measured at room temperature (*dashed line*) and 4 K (*solid line*). (**b**) Integrated photoluminescence intensity vs. temperature for the Si-rich oxide sample ($n = 1.7$, annealed for 1 h at 1,100°C) (*inset*). Si-rich oxide emission spectra measured at room temperature (*dotted line*), 125 K (*dashed line*), and 10 K (*solid line*).

This observation is also consistent with our analysis of Si nanocrystal formation through micro-Raman spectroscopy and transmission electron microscopy presented in Sect. 2.

### *3.2. Emission Sensitization Through Energy Transfer from Si-Rich Dielectrics*

In this section, we will discuss the sensitization of the emission from Er ions and PbS quantum dots by Si nanocrystals. This process allows for the fabrication of longer wavelength emission devices integrated on Si substrates for applications in optical telecommunications, biological imaging, and sensing.

#### 3.2.1. Er

The recent discovery of efficient energy transfer between Si nanocrystals and Er ions has initiated an entirely new approach that profits from both the advantages of quantum size effects in Si and rare earth doping, promising a route toward the integration of CMOS technology with 1.54 µm light sources [20–25, 64, 78]. In particular, Er-doped Si-rich oxide systems, where Er is incorporated through ion implantation [22, 23] or co-sputtering [21, 25, 64, 77] have been extensively investigated. We have prepared Er-doped Si-rich $SiO_2$ films through co-sputtering from Er and Si targets in an $O_2$/Ar atmosphere. After deposition, the films are annealed at various temperatures to simultaneously form Si nanocrystals and activate the Er emission. The Er concentration was measured through Rutherford Backscattering Spectroscopy.

In Fig. 6a, we show that when Er ions are doped into Si-rich oxide the Si nanocrystal emission is reduced and the Er emission is enhanced relative to Er:$SiO_2$ samples that do not contain Si nanocrystals. The 1.54-µm Er-related emission can be efficiently excited also by pumping out of the Er transition resonance, using a pumping wavelength (457 nm) where Er ions are nonabsorbing. The almost totally overlapping Er emission spectra, obtained under resonant (488 nm) and nonresonant (457 nm) pumping conditions, directly show that Er excitation in Er:Si-rich oxide is completely mediated by the Si-rich oxide dielectric matrix that efficiently transfers the excitation energy to the Er ions (Fig. 6b). At the same time, the excitation efficiency of Er is strongly enhanced by energy transfer from the Si-rich oxide matrix. Figure 6c, d show a measurement of the excitation cross section through a linear fit of the emission inverse rise time vs. pump photon flux of Er in Si-rich oxide and stoichiometric $SiO_2$, respectively. The excitation cross section of Er in Si-rich oxide is $9.05 \times 10^{-17}$ $cm^2$ which is almost 1,000× larger than the Er excitation cross section in $SiO_2$ of $1.10 \times 10^{-19}$ $cm^2$.

The typical mechanism used to explain energy transfer between Si nanocrystals and Er ions is Förster–Dexter nonradiative energy coupling with a transfer rate that is directly proportional to the donor (Si-rich oxide) emission rate [78]. This suggests that the maximum Er emission enhancement relative to Er:$SiO_2$ should be present for Si-rich oxide samples with the strongest Si nanocrystal emission. However, recent experimental observations have questioned the validity of this simple picture since strong Er emission enhancement is exhibited by samples

annealed at low temperatures (<800°C) [63, 64] which show no appreciable Si-rich oxide emission [65]. For a sample with 38 at% Si and an Er concentration of $1 \times 10^{20}$ cm$^{-3}$, Fig. 7 shows that the Er emission is maximized for an annealing temperature of 700°C which is 200°C lower than the optimum annealing temperature for Er:$SiO_2$ and 450°C lower than the annealing temperature that maximizes the Si nanocrystal emission. We have recently suggested that the efficient energy transfer observed for low temperature annealed Er:Si-rich oxide materials can be assisted by nonradiative defect states within the Si-rich oxide matrix bandgap [65].

Energy transfer from the Si-rich matrix to Er also has been demonstrated for Er:Si-rich nitride systems, opening the possibility to extend the emission wavelength range of Si-rich nitride optical devices to the strategically relevant 1.54 μm region. Similar to the case of Er:Si-rich oxide, we demonstrate that the Er emission spectra obtained under resonant (488 nm) and nonresonant (457 nm) pumping conditions (Fig. 8a) almost totally overlap, directly showing that the Er excitation in Er:Si-rich nitride is also completely mediated by the Si-rich nitride dielectric matrix [79]. However, the annealing temperature range which optimizes the Er emission in Si-rich nitride is different from that of Er:Si-rich oxide. Figure 8c

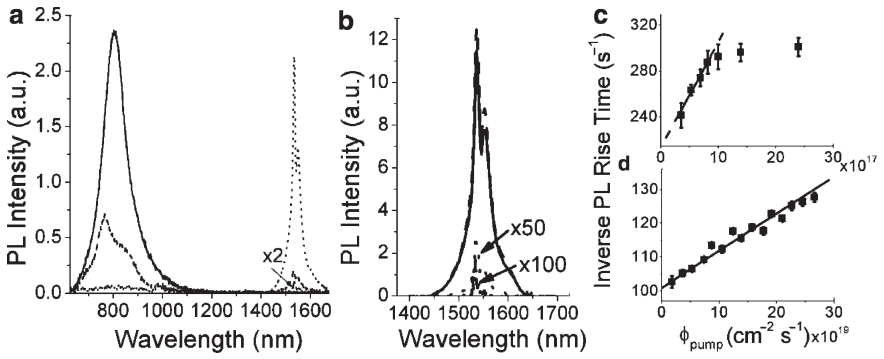


FIG. 6. (**a**) Room temperature photoluminescence vs. wavelength for a Si nanocrystals in $SiO_2$ sample with 38 at% Si annealed at 1,100°C (*solid line*), for an Er in Si-rich oxide sample with 38 at% Si and Er concentration of $8.2 \times 10^{19}$ cm$^{-3}$ annealed at 1,100°C (*dashed line*), for an Er in Si-rich oxide with 38 at% Si and Er concentration of $8.2 \times 10^{19}$ cm$^{-3}$ annealed at 600°C (*dotted line*), and an Er in $SiO_2$ sample with an Er concentration of $9 \times 10^{19}$ cm$^{-3}$ annealed at 1,100°C (*dashed-dotted line*, magnified by 2). (**b**) Room temperature Er emission for an Er:Si-rich oxide sample with 38 at % Si and an Er concentration of $8.2 \times 10^{19}$ cm$^{-3}$ annealed at 600°C. The emission spectrum was collected under 488-nm resonant excitation (*solid line*) and nonresonant 457-nm excitation (*dashed-dotted line*). Er in $SiO_2$ emission for a reference sample with an Er concentration of $9 \times 10^{19}$ cm$^{-3}$ annealed at 600°C under 488-nm resonant excitation (*dotted line*, magnified by 50) and under 457-nm nonresonant excitation (*dashed-dotted line*, magnified by 100). (**c**) Er emission inverse rise time vs. pumping photon flux at 488 nm for the Er:Si-rich oxide sample annealed at 600°C and containing $8.2 \times 10^{19}$ cm$^{-3}$ Er atoms and 38 at% Si. The *solid line* is a linear fit yielding an excitation cross section of $\sigma_{exc} = 9.05 \times 10^{-17}$ cm$^2$. (**d**) Er emission inverse rise time vs. pumping photon flux at 488 nm for the reference Er sample in $SiO_2$ annealed at 1,100°C with an Er concentration of $9 \times 10^{19}$ cm$^{-3}$. The *solid line* is a linear fit yielding an excitation cross section of $\sigma_{exc} = 1.10 \times 10^{-19}$ cm$^2$.

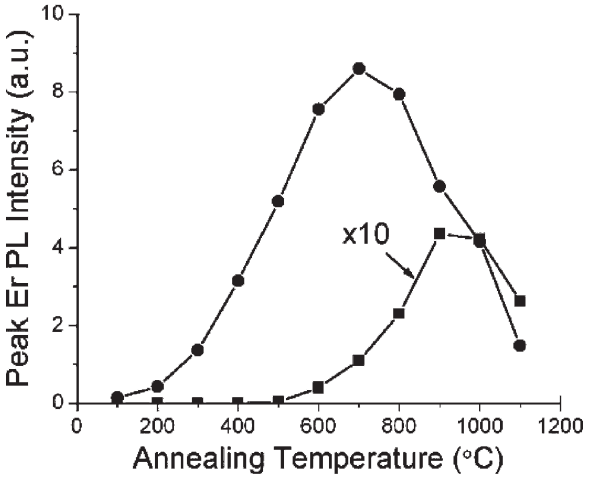


FIG. 7. Room temperature Er emission vs. annealing temperature for Er:Si-rich oxide samples with 38 at % Si and Er concentration of $8.2 \times 10^{19}$ cm$^{-3}$ (*circles*) and reference Er in $SiO_2$ samples with Er concentration of $9 \times 10^{19}$ cm$^{-3}$ (*squares*, magnified by 10).

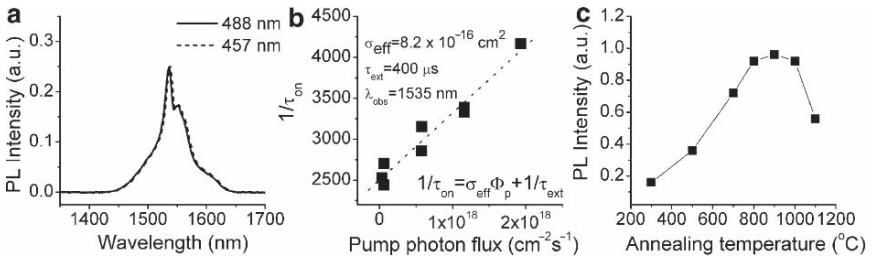


FIG. 8. (**a**) Resonant vs. nonresonant photoluminescence for Er:Si-rich nitride, produced by direct co-sputtering, with an index of refraction of 2.2 annealed at 900°C for 10 min. (**b**) Inverse Er emission rise time vs. pump photon flux for the Er:Si-rich nitride sample with an index of refraction of 2.2 annealed at 900°C for 10 min (*squares*). Linear fit of the inverse rise time data yielding an excitation cross section of $8.2 \times 10^{-16}$ cm$^2$ and an emission lifetime of 400 μs (*dashed line*). (**c**) Er photoluminescence intensity vs. annealing temperature for Er:Si-rich nitride films with an index of refraction of 2.2 and a fixed annealing time of 10 min.

shows the optimization of the Er emission in Si-rich nitride vs. annealing temperature. We have found that the Er emission is maximized for annealing temperatures in the range of 800–1,000°C, which is slightly higher than the optimum annealing temperature range for the Er in Si-rich oxide samples described above. The excitation cross section measured for the best emitting sample (Fig. 8b) was $8.2 \times 10^{-16}$ cm$^2$ which is one order of magnitude greater than the value measured for Er in Si-rich oxide. Additional experiments to understand both the origin and the efficiency of this transfer mechanism are currently in progress.

### 3.2.2. PbS Quantum Dots [66]

Colloidal quantum dots [80] are optoelectronic materials synthesized in, and suspended in, the solution phase. Because they may be dispersed in a solvent, they are readily coated onto an arbitrary substrate – semiconductor (crystalline or amorphous), dielectric (rigid or flexible) – at room temperature.

This convenient processing has already been widely exploited, for example in the PbS colloidal quantum dot materials system, to produce photodetectors and photovoltaics [81], electroluminescent devices [82], electro-optic modulation [83], and waveguides producing net modal gain in the 100 $cm^{-1}$ range [84].

The bulk bandgap of PbS, augmented through quantum size-effect tuning, ensures that quantum dot absorption and emission may readily be tuned between 850 and 1,800 nm through synthetic control over quantum dot diameter. As a result, PbS quantum dots are of great interest to enable optical signal production, detection, and modulation relevant to communications and inter-/intrachip interconnects.

A significant challenge remains to find a robust way to exchange information between colloidal quantum dots and Si electronics. Electronic transport across the Si–PbS interface may be possible. Here, however, we consider experimentally the possibility of long-range energy transfer – Förster transfer – between excitons in Si-rich nitride and PbS quantum dots.

The PbS quantum dots used to investigate energy transfer were produced using well-established colloidal synthesis techniques. As synthesized, each PbS quantum dot is capped by a layer of oleate ligand. To enhance the interaction strength between the PbS quantum dot and their surrounding materials, the 2-nm-long oleate ligands are replaced by the 0.5-nm-long butylamine ligands through a solution-based procedure. A proximately coupled donor–acceptor sample (Fig. 9, inset Sample A) was prepared by spin-coating five monolayers of PbS quantum dot (about 25 nm film thickness) on 50 nm of Si-rich nitride grown on a transparent quartz substrate. The reference sample (Fig. 9, inset Sample B) was identical except that the quantum dots were spin-cast onto a transparent quartz substrate. In the donor–spacer–acceptor structure (Fig. 9, inset Sample C), a 1-mm transparent quartz spacer was introduced between the PbS quantum dot acceptor layer and the 50 nm Si-rich nitride donor layer to prevent short-range dipole coupling while still allowing radiative coupling.

The energy transfer process was examined using a photoluminescence excitation experiment. The excitation wavelength was varied between 390 and 560 nm while the detection wavelength was fixed at the PbS quantum dot emission peak. Photoluminescence excitation spectra of the samples along with the Si-rich nitride absorption spectrum are shown in Fig. 9. For excitation wavelengths longer than 500 nm, where the Si-rich nitride absorption is negligible, the photoluminescence excitation spectra overlap for all samples. This is the regime of direct PbS quantum dot excitation alone, producing conventional photoluminescence. For excitation at wavelengths shorter than 500 nm, the photoluminescence of the proximately coupled donor–acceptor sample rises significantly, while the reference sample and the

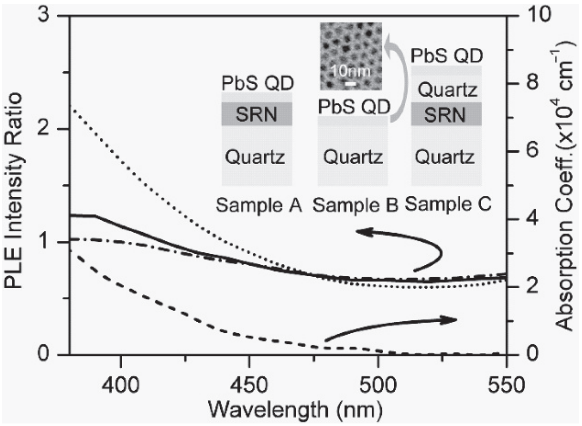


FIG. 9. (*Inset*) Schematic of the sample used to investigate energy transfer from Si-rich nitride to PbS quantum dots: (Sample A) The proximately-coupled donor-acceptor sample; (Sample B) The acceptor only reference sample; and (Sample C) The donor–spacer–acceptor sample. Above the schematic of Sample B we show a transmission electron microscope image of the PbS quantum dots with an average diameter of 5 nm. Photoluminescence excitation trace of the proximately coupled donor-acceptor sample (*dotted line*), the acceptor-only reference sample (*solid line*), and the donor–spacer–acceptor sample (*dashed-dotted line*). The absorption spectrum of a 50-nm thick Si-rich nitride (SRN) film (donor) on a quartz substrate is also shown (*dashed line*).

donor–spacer–acceptor sample overlap one another. Since the enhancement of the PbS emission closely follows the Si nanocrystal absorption it is concluded that the factor-of-two luminescence enhancement of PbS quantum dots coupled to the Si-rich nitride thin film donor is dominated by a short distance, nonradiative energy transfer process. This finding points to the possibility of a convenient coupling and thus monolithic integration of solution-processible, near-infrared-active optoelectronic materials on the electronics platform of CMOS Si.

## 4. DEVICES

The key components required to achieve devices based on Si nanocrystals are (1) optical confinement for waveguide-based edge emitting devices, (2) electrodes and electrical injection for electrically driven devices, and (3) resonant structures for lasing. The simplest structure for optical confinement and edge emitting devices is a planar optical waveguide, which consists of a high index waveguide layer on a low-index undercladding layer. Light is confined in one dimension within the waveguide layer through total internal reflection from the air-waveguide and undercladding-waveguide interfaces. Light amplification and optical gain as large as 100 $cm^{-1}$ have been demonstrated in these devices [14, 17, 18, 85]. Two-dimensional confinement can be achieved through patterning of the waveguide

layer through photolithography and reactive ion etching techniques. The two-dimensional confinement allows for the fabrication of bends [86], splitters [86], directional couplers [87], and ring resonators [88, 89]. Light amplification through pump and probe techniques has been reported in Er-doped Si nanocrystal waveguides [90, 91].

Several studies have been devoted toward developing efficient and stable electrically pumped light emission in Si nanocrystals embedded in Si-rich $SiO_2$ [61, 92]. Electrical excitation could prove to be more efficient than optical excitation due to the experimentally measured 500× increase in the electrical excitation cross section with respect to optical excitation cross section [93]. However, electroluminescent devices are limited due to the presence of the stoichiometric oxide separating Si nanocrystals, which acts as a barrier to the flow of electrical current. Careful control of the size and density of Si nanocrystals is required to achieve efficient injection via a Fowler–Nordheim tunneling process across the oxide barriers [61]. The identical behavior observed for devices under forward and reverse bias suggests that the excitation mechanism is one of impact ionization [61], which can lead to device degradation and failure. Very recently, Walters et al. [94] have demonstrated a field effect injection scheme where electrons and holes are injected into the active region through the same channel using a sequential programming process allowing for improved control of the injection process and improved device stability. Si-rich nitride has also been proposed as an alternative host to improve the electrical properties since the Si nitride barriers have a smaller bandgap which facilitates tunneling between nanocrystals [32, 33].

All of the structures described above are appropriate for the fabrication of amplifiers or light emitting diodes. To achieve laser operation the Si nanocrystal gain medium must be inserted into an optical microcavity through the use of Bragg gratings or a ring resonator. For laser oscillations to start the single pass gain must equal the total loss of the cavity requiring careful control of materials properties and device fabrication. An alternative approach is the use of aperiodic complex photonic structures. In these structures, multiple light reflections induce an "almost random" dielectric environment causing the diffusion of light waves to undergo a power-law (weak) localization. Large field enhancement at specific frequencies corresponding to perfect transmission states (resonant transmission) also occurs [95, 96].

We describe the fabrication of electrically driven light emitting diodes and optically pumped complex photonic structures based on PECVD-deposited Si-rich nitride in the following sections.

### *4.1. Si-Rich Nitride Light Emitting Diodes*

In Sect. 3, we discussed light emission from Si nanocrystals under optical excitation. However, for integration with Si microelectronics electrically driven light emitting devices are more advantageous.

Electrical *I–V* measurements can be used to evaluate the performance of our PECVD deposited Si-rich nitride films for electroluminescent devices. The device tested is shown schematically in Fig. 10a where a Si-rich nitride film was deposited on a $p^{++}$-Si substrate with Au top and bottom contacts. In Fig. 10b, we show the

electrical *I–V* characteristics of the Si-rich nitride devices where we have discovered that the electrical properties of Si-rich nitride films are dramatically enhanced after the postdeposition annealing treatments [79]. The conductivity of our devices is improved by more than two orders of magnitude after annealing for 10 min at 700°C (Fig. 10b), with high current densities achieved at 5 V through 700-nm thick light emitting films. This behavior is consistent with hopping conduction through percolation clusters of empty localized states that can be associated both to the amorphous Si-rich nitride matrix and to the Si nanocrystal interfaces. Since the postdeposition annealing treatment has a dramatic effect on electrical transport of Si-rich nitride films, the onset of a conduction percolation threshold is associated with the higher density of crystalline Si clusters [97] achieved through our annealing conditions.

After the demonstration of efficient electrical injection in our Si-rich nitride-based luminescent films we studied the electroluminescence properties. A different structure, shown schematically in Fig. 11b, was used to test the electroluminescence, where the Au top contact is replaced by a transparent ITO layer deposited by sputtering and the substrate doping is switched from $p^{++}$-Si to $n^{++}$-Si. The $n^{++}$-Si

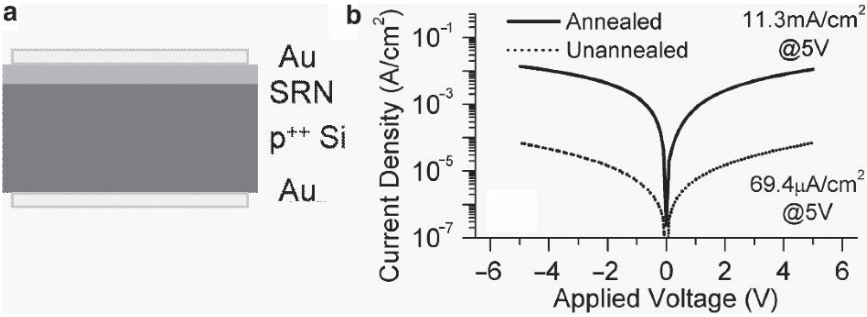


FIG. 10. (**a**) Schematic diagram of the Si-rich nitride device. (**b**) *I–V* characteristics of the Si-rich nitride device with annealing (10 min, 700°C, *solid line*) and without annealing (*dotted line*).

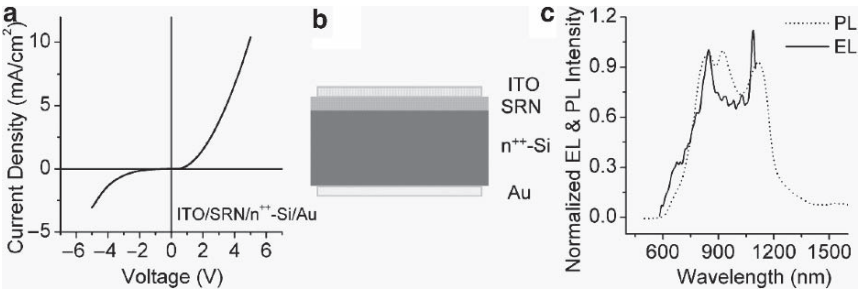


FIG. 11. (**a**) *I–V* characteristics for the structure of ITO/Si-rich nitride/$n^{++}$-Si/Au. (**b**) Schematic of the p–i–n structure used to investigate the electroluminescence. (**c**) Normalized room temperature photoluminescence (*dotted line*) and electroluminescence (5 V forward bias, *solid line*) for ITO/Si-rich nitride/$n^{++}$-Si/Au.

substrate was chosen after the transport characteristics for devices deposited on $p^{++}$-Si substrates showed a unipolar behavior (the ITO is a hole supplier) with no electroluminescence detectable at room temperature. When ITO coated Si-rich nitride devices are deposited on $n^{++}$-Si substrates (Fig. 11a), a vertical p–i–n structure is formed and the *I–V* characteristics show typical diode behavior with room temperature electroluminescence observed under 5 V forward bias [79]. The electroluminescence signal overlapped spectrally with the Si-rich nitride photoluminescence spectrum within the sensitivity range of the detector (Fig. 11c). The observation of electroluminescence at low voltages and the requirement of a p–i–n bipolar injection scheme suggest that the electroluminescence results from electron–hole recombination and not impact ionization. Further experiments are in progress to understand the mechanism of electrical injection and optimize the electroluminescence of our Si-rich nitride systems.

### *4.2. Si-Rich Nitride Light Emitting Complex Photonic Structures*

Periodic Bragg gratings and multilayer structures are well known for their application in laser cavities and antireflection coatings. When used in laser cavities they provide the optical feedback required to achieve lasing. Photonic quasicrystals are an alternative to achieve strong field enhancement and enhanced emission. Photonic quasicrystals are deterministically generated dielectric structures with a nonperiodic refractive index modulation. The several classes of photonic quasicrystals represent an intermediate organization stage between periodic dielectric materials, namely photonic crystal structures [98–100], and random media [101–104]. Photonic quasicrystals show peculiar physical properties like the formation of multiple frequency gap regions called pseudobandgaps [105, 106], the presence of fractal transmission resonances with local field enhancement [107, 108], and the occurrence of "critically" localized states [109, 110]. We have focused on aperiodic quasicrystals based on the Thue–Morse sequence [111–113] that are generated according the rule $\sigma_{T-M}$: A→AB, B→BA [114]. The lower order Thue–Morse sequences are given by the strings: $S_0$ = A, $S_1$ = AB, $S_2$ = ABBA, $S_3$ = ABBABAAB, etc. Recently optical Thue–Morse quasicrystals have been demonstrated for the case of A = $SiO_2$ and B = Si [115]. If the Si layer is replaced with Si-rich nitride, the structure can be annealed to form light emitting centers embedded within the Thue–Morse sequence [31]. This approach can be used for the fabrication of CMOS-compatible active waveguides and complex photonic crystal structures for a variety of different applications ranging from innovative resonant structures for multiwavelength on-chip light amplification and lasing, to optical biosensing and dense optical wavelength division multiplexing (WDM).

We have recently fabricated the first light emitting Thue–Morse photonic multilayer structure by aperiodically arranging Si-rich nitride and $SiO_2$ layers grown by PECVD [31]. Figure 12a shows an SEM image of a 64-layer Thue–Morse structure fabricated from Si-rich nitride and $SiO_2$. The optical transmission spectra of a thermally annealed 64-layer Thue–Morse structure are shown in Fig. 12b, which shows the presence of several resonant transmission states within the typical Si-rich

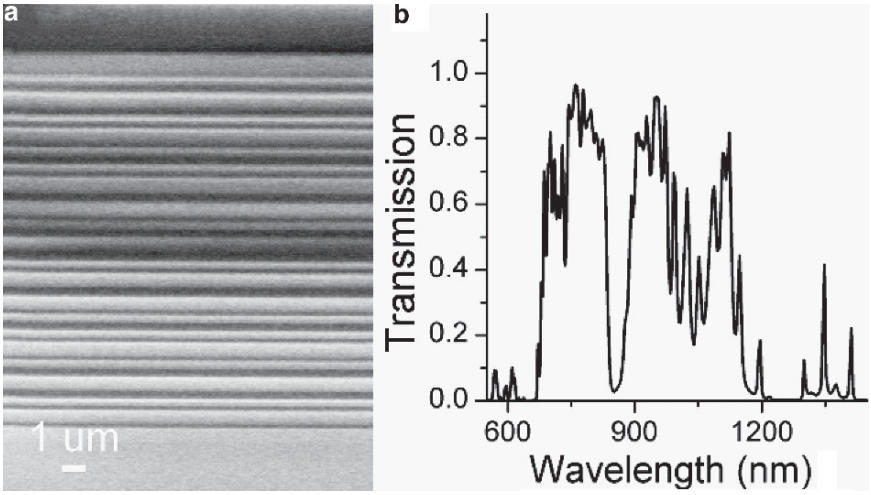


FIG. 12. (**a**) SEM image of a 64-layer Thue–Morse quasicrystal deposited on a $SiO_2$ substrate where the light layers are $SiO_2$ and the dark layers are Si-rich nitride. (**b**) Experimental transmission spectrum for the 64-layer Thue–Morse structure overlapping within the light-emission range of the Si-rich nitride material.

nitride emission band. These resonant transmission states have a dramatic effect on the Si-rich nitride emission spectrum. In Fig. 13a, we compare the emission spectra of a 64-layer Thue–Morse structure and a homogeneous Si-rich nitride reference sample with the same optical thickness. The presence of the aperiodic dielectric environment transforms the broad and featureless emission band characteristic of the Si-rich nitride reference sample by locally enhancing the emission with respect to the reference homogeneous Si-rich nitride sample at several narrow frequency states (emission spikes) induced by the Thue–Morse structure. Emission enhancement relative to the homogeneous sample of more than 5× can be achieved (Fig. 13b). A one-dimensional transfer matrix simulation of a Thue–Morse localized field state is shown in Fig. 13c. Field enhancement effects up to approximately ~30 times the incident field amplitude are predicted for a 64-layer Thue–Morse structure. Moreover, the localized character of these states is also reflected in the dramatic change of the angular emission profile of the Thue–Morse structure. Figure 13d shows the strongly directional light emission observed for the Thue–Morse structures at different wavelengths corresponding to localized states with field enhancement. For the Si-rich nitride homogeneous sample, an approximately Lambertian wide-angle emission profile was observed since all the states are delocalized with negligible field enhancement.

The demonstration of broadband light emitting Thue–Morse structures with highly directional and multiple wavelength emission enhancement effects can provide an attractive route toward the fabrication of optically active CMOS-devices for multi-wavelength operation.